This is a repository copy of *Analytical modeling of sheet carrier density and ON-resistance in Polarization Super-Junction HFETs*.

White Rose Research Online URL for this paper:
https://eprints.whiterose.ac.uk/178389/

Version: Accepted Version

Article:

Yan, H., Du, Y., Luo, P. et al. (2 more authors) (2021) Analytical modeling of sheet carrier density and ON-resistance in Polarization Super-Junction HFETs. IEEE Transactions on Electron Devices, 68 (11). pp. 5714-5719. ISSN 0018-9383

https://doi.org/10.1109/TED.2021.3115091

© 2021 IEEE. Personal use of this material is permitted. Permission from IEEE must be obtained for all other users, including reprinting/ republishing this material for advertising or promotional purposes, creating new collective works for resale or redistribution to servers or lists, or reuse of any copyrighted components of this work in other works. Reproduced in accordance with the publisher's self-archiving policy.

Reuse

Items deposited in White Rose Research Online are protected by copyright, with all rights reserved unless indicated otherwise. They may be downloaded and/or printed for private study, or other acts as permitted by national copyright laws. The publisher or other rights holders may allow further reproduction and re-use of the full text version. This is indicated by the licence information on the White Rose Research Online record for the item.

Takedown

If you consider content in White Rose Research Online to be in breach of UK law, please notify us by emailing eprints@whiterose.ac.uk including the URL of the record and the reason for the withdrawal request.

eprints@whiterose.ac.uk
https://eprints.whiterose.ac.uk/

Analytical Modeling of Sheet Carrier Density and ON-Resistance in Polarization Super-Junction HFETs

Hongyang Yan, Yangming Du, Peng Luo, *Member, IEEE*, Xiao Tan and Ekkanath Madathil Sankara Narayanan, *Senior Member, IEEE*

Abstract— **In this paper, we report on the analysis of the on-state behavior of Polarization Super-Junction (PSJ) HFETs. Theoretical models for calculating the sheet densities of Two-Dimensional Electron Gas (2DEG) and Two-Dimensional Hole Gas (2DHG) are proposed and calibrated with numerical simulations and experimental results. To calculate the area-specific on-state resistance ($R_{(on,sp)}$) of PSJ HFETs, Ohmic Gate (OG) structures are considered herein. The calculated results are well fitted with the simulated and measured results at different PSJ length (L_{PSJ}) conditions at room temperature.**

Index Terms—**Polarization Super Junction (PSJ), Heterojunction Field Effect Transistors (HFETs), area-specific on-state resistance ($R_{(on,sp)}$), Two-Dimensional Electron Gas (2DEG), Two-Dimensional Hole Gas (2DHG).**

I. Introduction

GALLIUM Nitride (GaN) is widely considered as the next generation pervasive power semiconductor material that can help to address global challenges of climate change, energy security, sustainability, and connectivity, due to its capability for high efficiency as well as high frequency. In integrated power conversion systems, due to the high concentration of a thin two-dimensional electrons realized through piezoelectric properties, AlGaN/GaN-based heterojunction field-effect transistors (HFETs) offer remarkable properties of low on-state resistance [1]. However, the trade-off between the area-specific on-state resistance ($R_{(on,sp)}$) and the breakdown voltage has been hindered in GaN HFETs and therefore Field Plates (FP) have been introduced to enhance the breakdown voltage. Field plates suppress the crowding of electric field at the gate edge towards the drain [2-4] and enable increase in breakdown voltage. However, FP structure also increases the area of the device and cost of manufacture. To overcome this, Polarization Super Junction (PSJ) technology was proposed and has been applied on GaN HEMTs [5, 6]. The PSJ concept is based on the polarization property of III–V group nitride compound semiconductors to realize the co-existence of high-density two-dimensional electron gas (2DEG) and two-dimensional hole gas (2DHG) at the hetero-interfaces to realize charge balance [6]. The basic structure of the PSJ HFET, as shown in Fig. 1, arises from GaN/AlGaN/GaN double heterostructure which employs an inherent charge balance in the PSJ region. It can potentially break the one-dimensional material trade-off between the $R_{(on,sp)}$ and the breakdown voltage of conventional GaN technology [7]. This is because the electric field of the PSJ-HFETs features a rectangular shape in comparison to the triangular shape of the electric field distribution of conventional GaN FETs. Therefore, the breakdown voltage is purely determined by the PSJ length (L_{PSJ}) [5]. In addition, the L_{PSJ} is also key for the on-state behavior [7]. To optimize the on-state performance of PSJ HFET, particularly reducing the $R_{(on,sp)}$, the theoretical analysis of the 2DEG and 2DHG models is necessary.

In this paper, new analytical models are introduced to investigate the $R_{(on,sp)}$ of the Ohmic Gate (OG) PSJ HFET. Analytical models are calibrated with both simulated modes and experimental data to achieve accuracy.

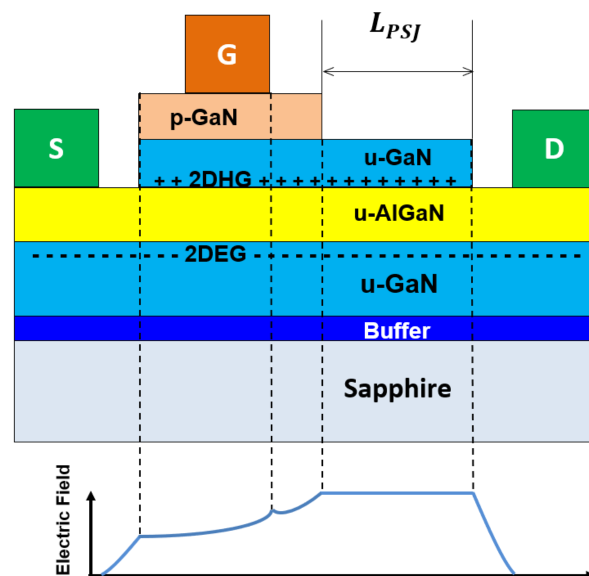

Fig. 1. Schematic cross-section and simplified electric field distribution of the Ohmic Gate (OG) PSJ HFET [7].

The authors are with the Electrical Machines and Drives Research Group, Department of Electronic and Electrical Engineering, The University of Sheffield, Sheffield S1 3JD, U.K. (e-mail: hyan8@sheffield.ac.uk; s.madathil@sheffield.ac.uk).

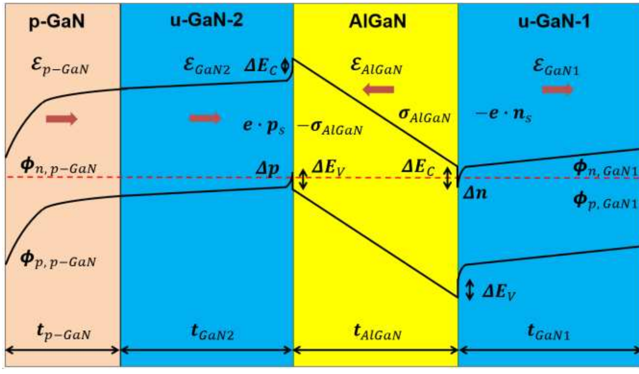

Fig. 2. Band diagram of p-GaN/u-GaN-2/AlGaN/u-GaN-1 heterostructure.

II. Methodology

Towards building analytical models, the first step is to calibrate the sheet density of 2DEG and 2DHG with the numerical simulation and experimental data [8, 9].

A. *Models for 2DEG and 2DHG*

In the analytical model, the structure used to calculate 2DEG and 2DHG sheet density is based on practical PSJ devices and reported samples [8, 9]. As shown in Fig. 2, it consists of a p-type doped GaN cap layer (p-GaN) with Mg-doped, an undoped GaN layer (u-GaN-2), an AlGaN layer and a u-GaN sub-layer (u-GaN-1). It was previously reported that 2DHG sheet density increased with the p-cap GaN layer thickness. However, when p-GaN layer thickness is beyond $20nm$, the influence of p-GaN layer thickness on 2DHG density becomes marginal [8]. Therefore, in the calibration process, each layer thickness is consistent with fabricated PSJ samples.

As shown in Fig. 2, to obtain expressions for sheet densities of 2DEG and 2DHG, the equation set (1)-(3) are built according to Gauss' law at the interface of p-GaN/u-GaN-2, u-GaN-2/AlGaN and AlGaN/u-GaN-1 [10, 11].

$$\epsilon_{p-GaN}\mathcal{E}_{p-GaN} - \epsilon_{GaN2}\mathcal{E}_{GaN2} = \sigma_{p-GaN} \quad (1)$$

$$\epsilon_{GaN2}\mathcal{E}_{GaN2} + \epsilon_{AlGaN}\mathcal{E}_{AlGaN} = \sigma_{AlGaN} - e \cdot p_s \quad (2)$$

$$\epsilon_{GaN1}\mathcal{E}_{GaN1} + \epsilon_{AlGaN}\mathcal{E}_{AlGaN} = \sigma_{AlGaN} - e \cdot n_s \quad (3)$$

In the equation set (Eqs. (1)-(3)) shown above, ϵ_{p-GaN}, ϵ_{GaN2}, ϵ_{AlGaN} and ϵ_{GaN1} are dielectric constants of p-GaN cap layer, u-GaN-2 layer, AlGaN layer and u-GaN-1 layer, respectively. $\mathcal{E}_{p-GaN}$, $\mathcal{E}_{GaN2}$, $\mathcal{E}_{AlGaN}$ and $\mathcal{E}_{GaN1}$ stand for the electric fields in the corresponding layers. σ_{p-GaN} and σ_{AlGaN} are the surface sheet charge of p-GaN layer and AlGaN layer. n_s and p_s represent the sheet carrier density of 2DEG and 2DHG. As shown in Fig. 2, considering the relationship in the band structure and band bending in the AlGaN region (yellow region), both electron and hole quantum wells (Δn and Δp) are satisfied the expression shown in Eq. (4) and can be simplified to Eq. (5).

$$t_{AlGaN}\mathcal{E}_{AlGaN} = \frac{1}{e}\left(E_{G,\ AlGaN} + \Delta p + \Delta n - \Delta E_V - \Delta E_C\right) \quad (4)$$

$$t_{AlGaN}\mathcal{E}_{AlGaN} = \frac{1}{e}(E_G + \Delta p + \Delta n) \quad (5)$$

Where t_{AlGaN} is the thickness of the AlGaN layer, $E_{G,\ AlGaN}$ and E_G are the bandgap of AlGaN and GaN layer, respectively. ΔE_V and ΔE_c are valence band and conduction band offsets between AlGaN layer and GaN layer [12].

To obtain expressions for n_s and p_s, it is necessary to further deduce equations from the band diagram shown in Fig. 2. With respect to the valance band potential from the right side to the left as shown in Fig. 2, one can derive the expression for the potential of the 2DHG quantum well as shown in Eq. (6). In a similar way, the expression of the 2DEG quantum well can be represented in Eq. (7) from the conduction band.

$$-\frac{\phi_{p,\ p-GaN}}{e} + t_{p-GaN}\mathcal{E}_{p-GaN} + t_{GaN2}\mathcal{E}_{GaN2} = \frac{\Delta p}{e} \quad (6)$$

$$\frac{\phi_{n,\ GaN1}}{e} - t_{GaN1}\mathcal{E}_{GaN1} = -\frac{\Delta n}{e} \quad (7)$$

Where t_{p-GaN}, t_{GaN2} and t_{GaN1} stand for p-GaN, u-GaN-2 and u-GaN-1 layer thickness, respectively. $\phi_{p,\ p-GaN}$ is the valance band barrier height of p-GaN cap and $\phi_{n,\ GaN1}$ is the conduction band barrier height of u-GaN-1 sub-layer. The following step is to substitute relations of $C_{p-GaN} = \frac{\epsilon_{p-GaN}}{t_{p-GaN}}$, $C_{AlGaN} = \frac{\epsilon_{AlGaN}}{t_{AlGaN}}$ and $C_{GaN1} = \frac{\epsilon_{GaN1}}{t_{GaN1}}$ into Eq. (6) and Eq. (7) and then revise equations to Eq. (8) and (9).

$$-\frac{\phi_{p,\ p-GaN}}{e} + \frac{\sigma_{AlGaN} - e \cdot p_s}{C} + \frac{\sigma_{p-GaN}}{C_{p-GaN}} - \frac{C_{AlGaN}}{eC} \times (E_G + \Delta p + \Delta n) = \frac{\Delta p}{e} \quad (8)$$

$$\frac{\phi_{n,\ GaN1}}{e} - \frac{\sigma_{AlGaN} - e \cdot n_s}{C_{GaN1}} + \frac{C_{AlGaN}}{eC_{GaN1}} \times (E_G + \Delta p + \Delta n) = -\frac{\Delta n}{e} \quad (9)$$

Where C_{p-GaN} , C_{AlGaN} and C_{GaN1} are the unit area capacitance of p-GaN, AlGaN and u-GaN-1 layer. C stands for the total unit area capacitance of p-GaN and u-GaN-2 layer.

$$n_s = \frac{m_{e1}}{\pi\hbar^2}\Delta n \quad (10)$$

$$p_s = \frac{m_{\mathrm{h}}}{\pi\hbar^2}\Delta p \quad (11)$$

According to the relationship between 2DEG sheet charge density and 2DEG quantum well, another approximate expression of 2DEG sheet density, as in Eq. (10), can be built into the model which can then be used to obtain n_s. In a similar way, an expression for p_s can also be derived as shown in Eq. (11) [11, 13].

$$\boldsymbol{n_s} = \frac{\left(-\frac{\phi_{p,\ p-GaN}}{e} + \frac{\sigma_{AlGaN}}{C} + \frac{\sigma_{p-GaN}}{C_{p-GaN}} - \frac{C_{AlGaN}E_G}{eC}\right)\left(\frac{C_{AlGaN}}{eC_{GaN1}} \cdot \frac{\pi\hbar^2}{m_h}\right) + \left(\frac{C_{AlGaN}}{eC} \cdot \frac{\pi\hbar^2}{m_h} + \frac{\pi\hbar^2}{em_h} + \frac{e}{C}\right)\left(\frac{\phi_{n,\ GaN1}}{e} - \frac{\sigma_{AlGaN}}{C_{GaN1}} + \frac{C_{AlGaN}E_G}{eC_{GaN1}}\right)}{\left(\frac{C_{AlGaN}}{eC} \cdot \frac{\pi\hbar^2}{m_e}\right)\left(\frac{C_{AlGaN}}{eC_{GaN1}} \cdot \frac{\pi\hbar^2}{m_h}\right) - \left(\frac{C_{AlGaN}}{eC} \cdot \frac{\pi\hbar^2}{m_h} + \frac{\pi\hbar^2}{em_h} + \frac{e}{C}\right)\left(\frac{C_{AlGaN}}{eC_{GaN1}} \cdot \frac{\pi\hbar^2}{m_e} + \frac{\pi\hbar^2}{em_e} + \frac{e}{C_{GaN1}}\right)} \quad (12)$$

$$\boldsymbol{p_s} = \frac{\left(\frac{C_{AlGaN}}{eC} \cdot \frac{\pi\hbar^2}{m_e}\right)\left(\frac{\phi_{n,\ GaN1}}{e} - \frac{\sigma_{AlGaN}}{C_{GaN1}} + \frac{C_{AlGaN}E_G}{eC_{GaN1}}\right) + \left(-\frac{\phi_{p,\ p-GaN}}{e} + \frac{\sigma_{AlGaN}}{C} + \frac{\sigma_{p-GaN}}{C_{p-GaN}} - \frac{C_{AlGaN}E_G}{eC}\right)\left(\frac{C_{AlGaN}}{eC_{GaN1}} \cdot \frac{\pi\hbar^2}{m_e} + \frac{\pi\hbar^2}{em_e} + \frac{e}{C_{GaN1}}\right)}{\left(\frac{C_{AlGaN}}{eC} \cdot \frac{\pi\hbar^2}{m_h} + \frac{\pi\hbar^2}{em_h} + \frac{e}{C}\right)\left(\frac{C_{AlGaN}}{eC_{GaN1}} \cdot \frac{\pi\hbar^2}{m_e} + \frac{\pi\hbar^2}{em_e} + \frac{e}{C_{GaN1}}\right) - \left(\frac{C_{AlGaN}}{eC} \cdot \frac{\pi\hbar^2}{m_e}\right)\left(\frac{C_{AlGaN}}{eC_{GaN1}} \cdot \frac{\pi\hbar^2}{m_h}\right)} \quad (13)$$

$$\boldsymbol{n_s} = \frac{\sigma_{AlGaN}}{e} - \frac{\phi_{n,\ GaN1} \cdot C_{GaN1}}{e^2} - \frac{C_{AlGaN}E_G}{e^2} \quad (14)$$

$$\boldsymbol{p_s} = \frac{\sigma_{AlGaN}}{e} + \frac{\sigma_{p-GaN} \cdot C}{eC_{p-GaN}} - \frac{\phi_{p,\ p-GaN} \cdot C}{e^2} - \frac{C_{AlGaN}E_G}{e^2} \quad (15)$$

Consequently, n_s and p_s expressions as presented in Eq. (12) and (13) can be derived by simultaneous Eqs. (1)-(13). In Eq. (12) and (13), the order of magnitude of some terms are much smaller than others ($\frac{e}{C_{AlGaN}} \gg \frac{\pi\hbar^2}{e \cdot m_e}, \frac{e}{C} \gg \frac{C_{AlGaN}}{eC_{GaN1}} \cdot \frac{\pi\hbar^2}{m_e}, \cdots$). These can be neglected during the simplification. Therefore, n_s and p_s expressions in the analytical model can be finally simplified to Eq. (14) and (15), respectively. Table. 1 shows related parameters and equations used in the calculation. For instance, σ_{AlGaN} is the sum of spontaneous polarisation charge (P_{sp}) and piezoelectric polarization charge (P_{pz}), which can be calculated from Table. 1.

TABLE I

PARAMETERS AND EQUATIONS USED FOR CALCULATION

Symbol	Unit	Value
$\epsilon_{Al_xGa_{1-x}N}$		$8.5x\epsilon_0 + 8.9(1-x)\epsilon_0$
ϵ_{GaN}		$8.9\epsilon_0$
$E_g(Al_xGa_{1-x}N)$	eV	$E_g(AlN)x + E_g(GaN)(1-x) - 1.3x(1-x)$
σ_{AlGaN}	C/m^2	$\lvert \Delta P_{sp} \rvert + \lvert \Delta P_{pz} \rvert$
$P_{sp}(GaN)$	C/m^2	-0.034
$P_{sp}(Al_xGa_{1-x}N)$	C/m^2	$(-0.09x - 0.034(1-x))$
$P_{pz}(Al_xGa_{1-x}N)$	C/m^2	$2\frac{a(x)-a_0}{a_0}\left(e_{31} - \frac{C_{13}}{C_{33}}e_{33}\right)$
$a(Al_xGa_{1-x}N)$	Å	$a(Al_xGa_{1-x}N) = 3.112x + 3.189(1-x)$
$a_0(GaN)$	Å	3.189
e_{31}	C/m^2	$-0.53x - 0.34(1-x)$
e_{33}	C/m^2	$1.5x + 0.67(1-x)$
C_{13}	Gpa	$127x + 100(1-x)$
C_{33}	Gpa	$382x + 392(1-x)$
m_0	kg	9.11×10^{-31}
$m_{e(Al_xGa_{1-x}N)}$		$(0.314x + 0.2(1-x))m_0$
$m_{h(Al_xGa_{1-x}N)}$		$(0.417x + 1.0(1-x))m_0$
ħ	$J \cdot s$	1.05×10^{-34}

Mg dopants do not influence the calculation of 2DEG and 2DHG [8, 9]. This is because $30nm$ of p-type doped GaN cap layer (p-GaN) with $5 \times 10^{19} cm^{-3}$ Mg doping concentration can only serve approximate $1.5 \times 10^{10} cm^{-2}$ positive sheet charge density when Mg active percentage is 1% [9]. Compared with both calculated and experimental results of nearly $10^{13} cm^{-2}$ 2DHG sheet density, the contribution from p-GaN layer is negligible.

In the numerical simulation model, physics-based solutions for the sheet density of 2DEG and 2DHG are

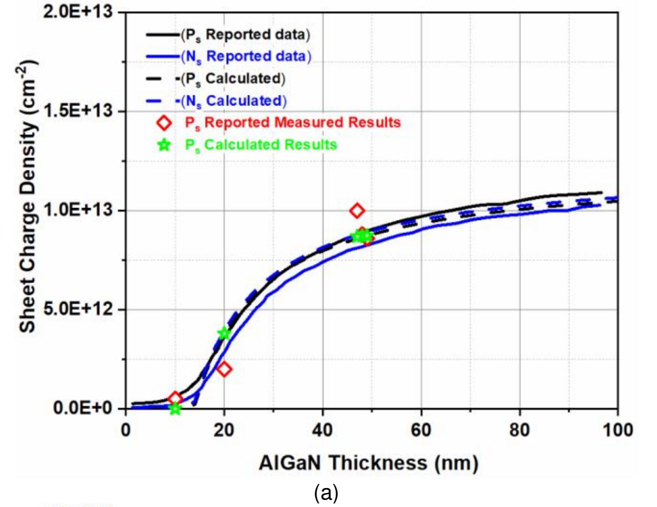

(a)

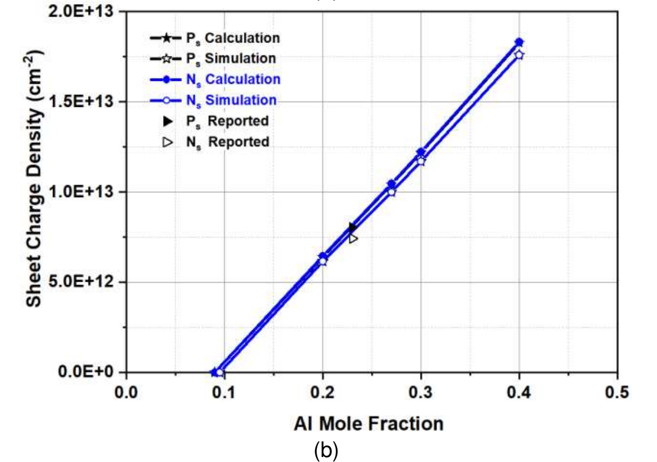

(b)

Fig. 3. (a) Reported results vs. calculated results of N_S and P_S as AlGaN thickness varies from 0 to $100nm$. The solid black line is the reported P_s and the solid blue line is the reported N_s. The dashed black and blue lines stand for the calculated P_s and N_s, respectively. Red rhombuses are reported measured results and green stars are calculated results [8, 9]. (b) Calculated and simulated predictions of N_S and P_S as Al mole fraction alters from 9% to 40% in the heterostructure.

TABLE II
DATA OF LAYER STRUCTURES

Sample (Al 23%)	Layer Thickness (nm)				$Reported$ P_S ($10^{13}cm^{-2}$)	$Calculated$ P_S ($10^{13}cm^{-2}$)
	t_{p-GaN}	t_{GaN2}	t_{AlGaN}	t_{GaN1}		
1	30	20	10	1500	0.05	0.00
2	30	20	20	1500	0.20	0.38
3	30	60	47	1500	1.00	0.87
4	30	20	48	1500	0.87	0.87
5	20	20	49	1500	0.86	0.87

achieved in Silvaco by using models such as POLAR (spontaneous polarisation), CALC.STRAIN (piezoelectric polarisation), CONSRH (Shockley-Read-Hall recombination using concentration-dependent lifetimes) and AUGER (recombination accounting for high-level injection effects) to obtain reliable results [14]. The models used in the simulation are based on default parameters. To simultaneously calibrate with PSJ HFET measurement results, parameters such as the thickness of PSJ layers and Al mole fraction are set as the same as those of fabricated PSJ devices.

Fig. 3 (a) compares the calculated prediction of N_s and P_s with reported measurement results at different AlGaN layer thicknesses. Parameters applied in analytical models, such as t_{p-GaN}, t_{GaN2}, t_{AlGaN} and t_{GaN1} listed in Table. 2, are adjusted to fit measured results (red rhombus) in the reference [8, 9]. The calculated results are close to the measurement results. Both N_s and P_s increase with the increase of the AlGaN layer thickness. Fig. 3 (b) shows the comparison of calculated prediction with the simulated prediction of N_s and P_s versus Al mole fraction. It can be found that both identical calculated and simulated results of N_s and P_s increase as Al mole fraction increases. Verified results are applied to both the analytical model and the simulated model in the following analysis of $R_{(on,sp)}$.

B. The analytical model for $R_{(on,sp)}$

Fig. 4 shows the schematic cross-section of the Ohmic Gate (OG) PSJ HFET [7]. The gate terminal is an ohmic contact formed on the p-GaN cap layer. At the gate region, the OG PSJ HFET consists of a $60nm$ p-type doped GaN cap layer with $5\times10^{19}cm^{-3}$ Mg dopants, a $65nm$ undoped GaN layer, a $40nm$ AlGaN layer and a $1\mu m$ u-GaN sub-layer. In the PSJ region, it consists of a $65nm$ undoped GaN layer, a $40nm$ AlGaN layer and a $1\mu m$ u-GaN sub-layer. To calculate $R_{(on,sp)}$ of OG PSJ HFET by the analytical model, based on the current flow direction along the dashed line under the on-state condition, it can be divided into four different regions (PSJ region, channel region, gap region and contact region) according to the differences in the sheet carrier densities and mobilities of 2DEG and 2DHG, as shown in Fig. 4. Therefore, the total specific on-state

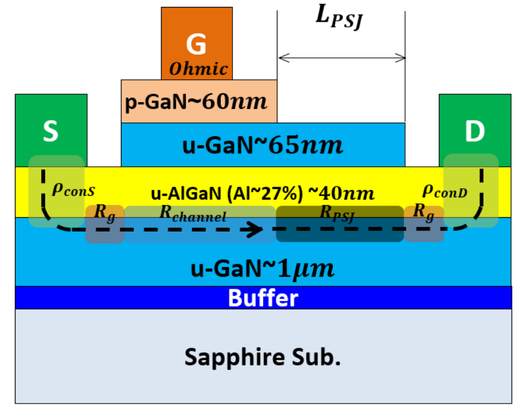

Fig. 4. Schematic device cross-section for calculating $R_{(on,sp)}$ of OG PSJ HFET

resistance ($R_{on}A$) can be considered as the sum of the PSJ region resistance (R_{PSJ}), the channel region resistance (R_{ch}) and the gap region resistance (R_g) multiplies device area (A) and then plus the contact resistivity (ρ_{cons} and ρ_{conD}) as shown in Eq. (16), assuming that device width is constant and applicable equally to all these parameters. Gap regions consist of the area between source and gate and the space between PSJ region and drain, as shown in Fig. 4. In PSJ HFET analytical models, to improve the fitting results, R_g cannot be ignored and need to be calculated separately.

$$R_{on}A = (R_{PSJ} + R_{ch} + R_g)\times A + \rho_{conS} + \rho_{conD} \tag{16}$$

The expression of R_{PSJ} can be derived in Eq. (17), where q is the electron charge and μ_{2DEG} is the mobility of 2DEG in the PSJ region. n_{2DEG} is the concentration of 2DEG. When integrate n_{2DEG} vertically by the height H, the result is 2DEG sheet density (σ_{2DEG}). σ_{2DEG} is calculated by the same method demonstrated in previous work. W stands for the width of the device.

$$R_{PSJ} = \frac{1}{qn_{2DEG}\mu_{2DEG}} \times \frac{L_{PSJ}}{H\times W} = \frac{L_{PSJ}}{q\mu_{2DEG}(n_{2DEG}\times H)W} = \frac{L_{PSJ}}{q\mu_{2DEG}\sigma_{2DEG}W} \tag{17}$$

In the gap region, the derivation of the PSJ region is repeated and the expression for R_g is derived from Eq. (18), where σ_{2DEG2} and μ_{2DEG2} are the sheet density and mobility of 2DEG in gap regions. L_g represents the total length of the gap region and is $7\mu m$ in OG PSJ HFET. 2DEG sheet density and mobility in gap regions (AlGaN/GaN) are different with those in the PSJ region (p-GaN/GaN/AlGaN/GAN). Therefore, both σ_{2DEG2} and μ_{2DEG2} are calculated again.

$$R_g = \frac{L_g}{q\mu_{2DEG2}\sigma_{2DEG2}W} \tag{18}$$

Considering that the OG PSJ HFET is an ohmic gate normally-on device and usually $V_g = 0V$ is applied on the

gate, the expression for R_{ch} in the PSJ HFET is demonstrated in Eq. (19), where L_{ch} is $5\mu m$ and represents the channel length and μ_{ch} is the carrier mobility in the channel. σ_{ch} is the sheet charge density of 2DEG in the channel.

$$R_{ch} = \frac{L_{ch}}{q\mu_{ch}\sigma_{ch}W} \tag{19}$$

ρ_{conS} and ρ_{conD} stand for the contact resistivity of the source and the drain electrode, respectively, which measured and calculated by transmission line method (TLM) as shown in Eq. (20).

$$\rho_{conS} = \rho_{conD} = R_C L_T W = 2.31 \times 10^{-2}\ m\Omega \cdot cm^2\ (TLM\ Testing) \tag{20}$$

Equations (16)-(20) are analytical models for analyzing and calibrating $R_{(on,sp)}$ with simulated and measured results. **In analytical models, considering the impact from traps, the sheet density (σ_{2DEG}) and the mobility (μ_{2DEG}) of 2DEG need to be adjusted with the experimental data to increase the accuracy. σ_{2DEG} and μ_{2DEG} both reduce after calibrating with experimental results since partial carriers (electrons), which have gained high kinetic energy after being accelerated by the electric field, are captured by traps.** The calculated $I_d - V_d$ characteristics based on analytical models are demonstrated in Fig. 5.

C. The simulated model for $R_{(on,sp)}$

The $R_{(on,sp)}$ of the simulated models is calculated from the simulated $I_d - V_d$ curves. Models and parameters are consistent with those previously mentioned 2DEG and 2DHG sheet density simulations. Fig. 5 presents simulated $I_d - V_d$ curves of OG PSJ HFETs. The cross-section of the device is shown in Fig. 4. The length of PSJ (L_{PSJ}) varies from $5\mu m$ to $20\mu m$. $V_g = 0V$ is applied on the gate as well as the source. In Fig. 5, at the point $V_d = 1V$ in the linear region, data is selected to obtain the simulated $R_{(on,sp)}$. It is obvious that $R_{(on,sp)}$ increases with L_{PSJ} increases.

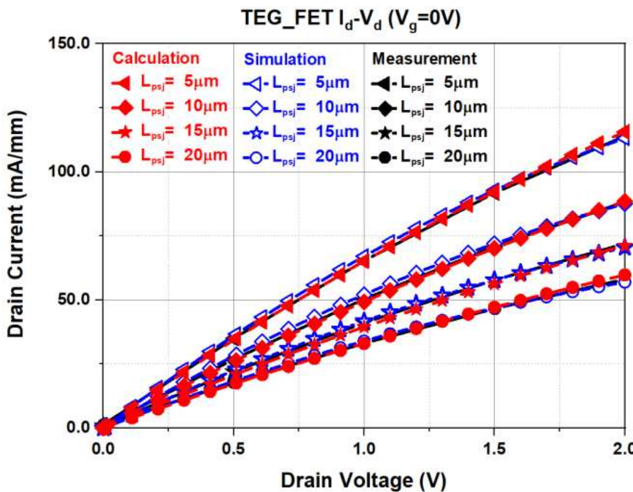

Fig. 5. Calculated, Simulated and Measured $I_d - V_d$ output characteristics of OG PSJ HFETs at $V_g = 0V$

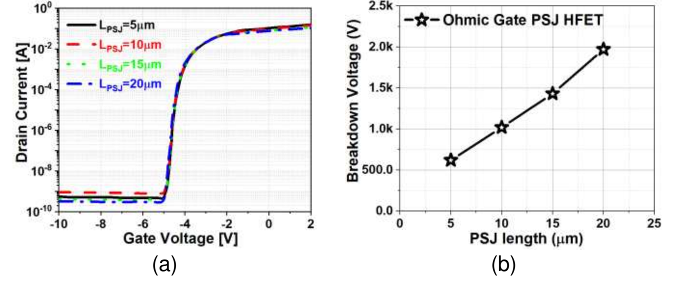

Fig. 6. Measured characteristics of OG PSJ HFETs when shifting L_{PSJ} from 5μm to 20μm (a) $I_d - V_g$ at $V_d = 10V$ (b) BV at $V_g = -15V$.

D. Measurement of fabricated PSJ HFETs

The measured $I_d - V_d$ curves of the fabricated OG PSJ HFETs are demonstrated in Fig. 5. The width of OG PSJ HFET samples is $1mm$. Similarly, measured results of $R_{(on,sp)}$ are obtained at the point of $V_d = 1V$. It can be found from Fig. 5 that the drain current reduces when L_{PSJ} is shifted from $5\mu m$ to $20\mu m$ at $V_g = 0V$ and $V_d = 1V$. **As can be seen in Fig. 5, the measured and simulated results show a divergence compared with the calculated results. This is caused by the self-heating effect, which is not accounted for. Therefore, the analytical model is mainly applicable to low voltage $R_{(on,sp)}$ analysis.** The saturation current reduces as the L_{PSJ} gets longer. Fig. 6 (a) is the $I_d - V_g$ characteristics of OG PSJ HFETs and Fig. 6 (b) presents that **the breakdown voltage of PSJ HFETs shows a linear increase with respect to the L_{PSJ} and an average breakdown field strength between $1 \sim 1.5MV/cm$. Compared with the previous work [6], the average BV electric field strength is increased because of the improvement in the quality of the materials and further optimizing the charge balance in the PSJ region.**

III. Results Analysis

For accurate calibration of results, identical $V_g = 0V$ is applied in both analytical modelling and numerical modelling as well as in the measurements. As presented in Fig. 7, both analytical and simulated $R_{(on,sp)}$ of PSJ HFETs shown in Fig. 4 are fitted with experimental results when altering PSJ length L_{PSJ} from $5\ \mu m$ to $20\ \mu m$. Whether by calculation, simulation, or measurement, $R_{(on,sp)}$ shows an upward linear trend with the increase in L_{PSJ}. Table. 3 shows each R_{on} component ratio to the total R_{on}. It should be addressed that the length of each region, which is related to the device area (A), is also an essential factor to $R_{on}A$.

Summarizing the partly statistic $R_{(on,sp)}$ data and differences between calculated and simulated results on measurement data, it should be noted that both the sheet density and mobility of 2DEG are adjusted in calculated and simulated models in order to improve the fitting with experiment results. All differences in Fig. 7 can be attributed to the fabrication misalignment between different processes, the random measurement error and the assumption that

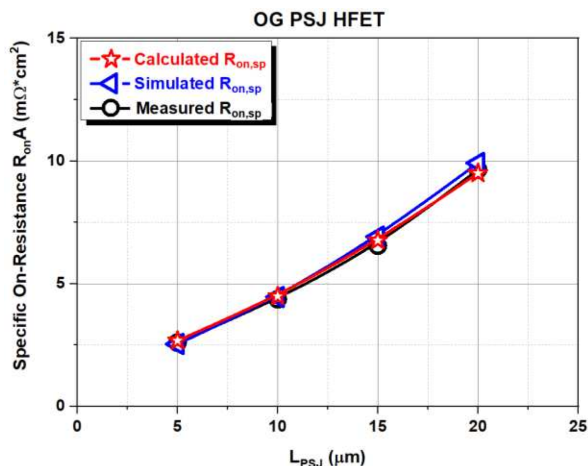

Fig. 7. Calculated, simulated, and measured $R_{(on,sp)}$ of OG PSJ HFETs at room temperatures when $V_g = 0V$.

TABLE III
EACH COMPONENT RATIO TO THE TOTAL RON IN ANALYTICAL MODEL

L_{PSJ} (μm)	Component Ratio (%)			R_{on} (Ω) (100%)	$\rho_{conS} + \rho_{conD}$ ($m\Omega \cdot cm^2$)	$R_{on}A$ ($m\Omega \cdot cm^2$)
	R_{PSJ}	R_g	R_{ch}			
5	29.4	41.2	29.4	15.8	0.046	2.68
10	45.5	31.5	22.7	20.4	0.046	4.49
15	55.6	25.9	18.5	25.1	0.046	6.77
20	62.5	21.9	15.6	29.7	0.046	9.50

2DEG mobility from each region in analytical models is constant. However, in the simulation and practical PSJ HFETs, the carrier mobility of 2DEG depends on different elements, such as the concentration and electric field distribution.

Analytical models in this work are mainly applied for the room temperature. With an increase in temperature, parameters, listed in Table. 1, and the carrier mobility will need to be readjusted with the experimental data to enhance the accuracy. Although analytical models have limitations from the constant assumption, reasonably accurate calculated results of $R_{(on,sp)}$ can still be obtained from these models. Analytical models provide an insight into the conduction mechanisms in PSJ HFETs and make contributions to optimize designs to reduce $R_{(on,sp)}$.

IV. CONCLUSION

Accurate analytical models for predicting the $R_{(on,sp)}$ of PSJ HFET are proposed and demonstrated. Dominant parameters for each region computing $R_{(on,sp)}$ are optimized in calculation and simulation. It clearly shows that calculated results fit with both the simulation and the experimental data of PSJ HFETs. They can also effectively assist in predicting the performance of PSJ devices precisely. Moreover, comprehensive analysis results establish a solid foundation to further optimize and improve PSJ device architectures.

ACKNOWLEDGMENT

The authors would like to thank Powdec KK, Japan for supplying some of the samples used in the analysis.

REFERENCES

[1] M. Asif Khan, A. Bhattarai, J. N. Kuznia, and D. T. Olson, "High electron mobility transistor based on a GaN - AlxGa1−xN heterojunction," *Applied Physics Letters,* vol. 63, no. 9, pp. 1214-1215, 1993, doi: 10.1063/1.109775.

[2] W. Saito *et al.*, "Field-Plate Structure Dependence of Current Collapse Phenomena in High-Voltage GaN-HEMTs," *IEEE Electron Device Letters,* vol. 31, no. 7, pp. 659-661, 2010, doi: 10.1109/led.2010.2048741.

[3] W. Saito, M. Kuraguchi, Y. Takada, K. Tsuda, I. Omura, and T. Ogura, "Design Optimization of High Breakdown Voltage AlGaN–GaN Power HEMT on an Insulating Substrate for RonA-VB Tradeoff Characteristics," *IEEE Transactions on Electron Devices,* vol. 52, no. 1, pp. 106-111, 2005, doi: 10.1109/ted.2004.841338.

[4] W. Saito *et al.*, "High breakdown voltage AlGaN-GaN power-HEMT design and high current density switching behavior," *IEEE Transactions on Electron Devices,* vol. 50, no. 12, pp. 2528-2531, 2003, doi: 10.1109/ted.2003.819248.

[5] A. Nakajima, K. Adachi, M. Shimizu, and H. Okumura, "Improvement of unipolar power device performance using a polarization junction," *Applied Physics Letters,* vol. 89, no. 19, 2006, doi: 10.1063/1.2372758.

[6] A. Nakajima, Y. Sumida, M. H. Dhyani, H. Kawai, and E. M. Narayanan, "GaN-Based Super Heterojunction Field Effect Transistors Using the Polarization Junction Concept," *IEEE Electron Device Letters,* vol. 32, no. 4, pp. 542-544, 2011, doi: 10.1109/led.2011.2105242.

[7] H. Kawai *et al.*, "Low cost high voltage GaN polarization superjunction field effect transistors," *physica status solidi (a),* vol. 214, no. 8, 2017, doi: 10.1002/pssa.201600834.

[8] A. Nakajima, Y. Sumida, M. H. Dhyani, H. Kawai, and E. M. S. Narayanan, "High Density Two-Dimensional Hole Gas Induced by Negative Polarization at GaN/AlGaN Heterointerface," *Applied Physics Express,* vol. 3, no. 12, 2010, doi: 10.1143/apex.3.121004.

[9] A. Nakajima *et al.*, "Generation and transportation mechanisms for two-dimensional hole gases in GaN/AlGaN/GaN double heterostructures," *Journal of Applied Physics,* vol. 115, no. 15, 2014, doi: 10.1063/1.4872242.

[10] T. R. Prunty, J. A. Smart, E. M. Chumbes, B. K. Ridley, L. F. Eastman, and J. R. Shealy, "Passivation of AlGaN/GaN heterostructures with silicon nitride for insulated gate transistors," *Proceedings of the IEEE/Cornell Conference on High Performance Devices,* pp. 208–214, IEEE, 2000.

[11] H. Hahn *et al.*, "Charge balancing in GaN-based 2-D electron gas devices employing an additional 2-D hole gas and its influence on dynamic behaviour of GaN-based heterostructure field effect transistors," *Journal of Applied Physics,* vol. 117, no. 10, 2015, doi: 10.1063/1.4913857.

[12] A. Kumar and M. M. De Souza, "Modelling the threshold voltage of p - channel enhancement - mode GaN heterostructure field - effect transistors," *IET Power Electronics,* vol. 11, no. 4, pp. 675-680, 2018, doi: 10.1049/iet-pel.2017.0438.

[13] O. Ambacher *et al.*, "Pyroelectric properties of Al(In)GaN/GaN hetero- and quantum well structures," (in English), *J Phys-Condens Mat,* vol. 14, no. 13, pp. 3399-3434, Apr 8 2002, doi: 10.1088/0953-8984/14/13/302.

[14] 'Silvaco TCAD Atlas', Version V3.44.1R, 2017. Available at https://www.silvaco.com/products/tcad.html, last accessed 24th November 2017.

[15] H. Morkoc and J. Leach, "Polarisation in GaN Based Heterostructures and Heterojunction Field Effect Transistiors (HFETs)," *Polarisation Effects in Semiconductors, Eds. New York : Springer,* pp. 373-457, 2008.